DEPARTAMENT D'ASTRONOMIA I METEOROLOGIA

UNIVERSITAT DE BARCELONA

Near-relativistic electron events. Monte Carlo simulations of solar injection and interplanetary transport

Memòria presentada per
Neus Àgueda Costafreda
per optar al grau de Doctora
per la Universitat de Barcelona.
Barcelona, 20 de febrer de 2008

7 Discussion

7.1 Comments on the method

We have developed a transport model to simulate the propagation of solar NR electrons in the interplanetary medium, including adiabatic focusing, pitch-angle dependent scattering and solar wind effects. This model provides near-Earth differential intensities in terms of Green's functions for particle transport normalized to one particle injected per steradian at the solar surface.

In order to compare the results of the transport model with observational data, we have developed a procedure to calculate the angular response function of sectors swept by a detector on board a spin-stabilized spacecraft. The analysis of sectored intensities rather than only spin-averaged time-intensity profiles is crucial for deriving both the scattering conditions and the injection profile. Without this sectored information, the effects of prolonged injection cannot be clearly separated from diffusive delays in the interplanetary medium. Our method to compute the angular response of the sectors allows for an estimation of the view boundaries of the telescope, that is, the highest and the lowest pitch-angle cosine of the particles being scanned, as a function of the orientation of the IMF vector. We have defined the pitch-angle cosine coverage of the telescope, μ-co, as the percentage of the pitch-angle cosine range scanned by the telescope (section 2.4.4).

We have applied our method to the sectored data of the LEFS60 telescope of the EPAM instrument on board *ACE* that measures electrons from 45 to 312 keV. By combining the results of the particle transport model with the angular response function of the LEFS60 sectors, we have been able to obtain sectored Green's functions for particle transport (section 2.4.5). The calculation of sectored Green's functions has allowed us to develop a method to deconvolve observational sectored intensities by means of a non-negative least squares method and to objectively derive the best fit, without relying on user evaluation.

We have tested the deconvolution procedure and found that, in order to discern the actual scattering conditions and the injection profile of SEPs released at the Sun from the LEFS60 sectored measurements, it is required that (a) the event is observed with μ-co $\geq 70\%$; and

(b) the telescope scans particles propagating antisunward along the field direction. These requirements are important when analyzing particle events measured by detectors on board spacecraft whose spin axis is not perpendicular to the ecliptic plane (as the case of the *ACE* spacecraft) or when the IMF has a large altitude component for a long time interval.

Conditions under which the application of the deconvolution algorithm provides reliable results have also been studied (sections 4.2 and 4.3). In particular, we have studied how measurement errors, or assuming an inadequate scattering model, can affect the results of the deconvolution. We have shown that if the magnetic field measurements were affected by systematic errors, for example, in one of the field components the injection profile resulting from the deconvolution would show fluctuations and previous spurious injection episodes of small intensity. In the case of statistical uncertainties in the intensity measurements, the resulting injection profile shows even higher fluctuations and noticeable intermittency. On the other hand, an inadequate scattering model could yield to an underestimation of the radial mean free path; furthermore the resulting injection profile would be delayed and affected by strong intermittency (as can be seen in Figure 4.7).

Ruffolo et al. (1998) and Maia et al. (2007) have addressed the problem of deconvolving the effects of interplanetary transport on observed intensities of SEPs, but they have used averaged intensities together with first-order anisotropy profiles to find out the best fit parameters. By using all the information contained in the sectored intensities our model allows us to deconvolve the effects of the interplanetary transport on the observed intensities and to deduce the injection profile of solar NR electrons. Special care has been taken on the values of the μ-co throughout the event since the observed sectored angular distributions cannot be representative of the actual PADs when the μ-co is low. The deconvolution technique presented in this work could be applied to survey the injection profiles and the scattering conditions in the interplanetary medium for a variety of events, as Ma Sung & Earl (1978) did, and thus deduce averaged properties of the interplanetary medium and the solar NR electron events.

In the present study, the longest time period selected for modelization is of four hours, comprising the onset, the peak and the beginning of the decay phase of the NR electron time-intensity profiles. For each event, the period selected for modelization was chosen as a compromise between computing time requirements and the validity of the scenario (injecting source close to the Sun, stable IMF and solar wind). Nevertheless, the modelization of individual events might be extended to longer time periods in the future.

In the model we have assumed a fixed solar source. However, in the case that we had to study NR electron events for longer time periods (> 4 h), we would have to consider the motion of the source, if it is related to a CME-driven shock. In the present study, we have

neglected this motion, since observed CMEs traveled not far from the Sun during the modeled periods; the release of NR electrons can be considered to happen near the Sun. This point has been discussed with some detail in the analysis of the Dec01 event (section 6.2.3). We concluded that, with the temporal constraints adopted for the time intervals analyzed (< 4 h), the potential error is small.

A point to be explored in the future is the goodness of the fit estimator, ζ (section 4.1.3). In fact, at first sight, this estimator resembles to a minimum χ^2 estimator but applied to logarithmic values. As far as we know, there is no mathematical or statistical studies in which the use of ζ can rely. From the test performed, it is clear that ζ is a sensitive estimator, at least to the purposes of our model, but its strength is solely based on the empirical test performed. It would be worth of consideration the analysis of other estimators able to take into account the difference of magnitude between the peak and the decay sectored intensities (sometimes higher than one order of magnitude) and the intensities measured in different energy channels. The ζ-values derived for different scattering models sometimes are too similar; compare, for example, in Table 5.6, the values of ζ for the μ-dependent scattering cases with $\epsilon = 0.10$ with that for $\epsilon = 0.01$. Fortunately, the obtained λ_r values are robust, in the sense that they are only weakly dependent on the scattering model adopted. But, for a full focused particle scattering model study, it is not absolutely clear if such aforementioned small differences between the ζ-values allow us to make strong statements about the type of scattering at work (which is different from the assumption that the lowest ζ-value identifies the better fit).

Analysis of data from the *STEREO* dual spacecraft observatories will help to further elucidate the role that CMEs and flares play in SEP events. Moreover, the future *HELEX* mission will represent further qualitative progress because it will provide particle measurements from the inner heliosphere where transport effects will be reduced. In order to derive as much information as possible from the particle detectors on board these spacecraft, it is essential to register not only time-intensity histories but also angular distributions of the observed particle populations. The analysis of these measurements should be combined with a careful study of the angular response of the detectors together with observations of radio, visible and hard X-ray emissions of the corona.

7.2 Discussion of the results

Early observations of 2–100 keV electron events at 1 AU suggested that the acceleration occurs in solar flares accompanied by type III radio bursts produced by beams of escaping electrons (Lin 1985). Later studies (Krucker et al. 1999; Haggerty & Roelof 2002), based on *Wind*/3DP and *ACE*/EPAM observations, respectively, indicated that in most events the

derived solar release time of >25 keV electrons was delayed with respect to the type III burst time by up to half an hour. Several authors (Maia & Pick 2004; Kahler et al. 2005; Klein et al. 2005; Simnett 2005a; Kahler et al. 2007) have focused on the comparison between the solar electron release times and the corresponding electromagnetic (X-rays, white-light and radio) signatures of the associated solar event. These studies have assumed that the electrons first observed at 1 AU of propagated scatter-free from the Sun and were injected simultaneously at all energies.

Petrosian & Liu (2004) and Liu et al. (2006) have described a plausible mechanism for particle acceleration in the solar corona, consisting in stochastic acceleration by (weak) MHD turbulence, that accounts for both electron and ^{3}He enhancements. In this scenario, particle acceleration is a fast process following the generation of turbulence by the release of magnetic energy during the flare. From the analysis of large SEP events and in-situ observations in the near-Earth space, it is known that shock waves are also efficient particle accelerators (see, for example, Cliver & Ling 2007 and references therein). As magnetic reconnection can generate super-fast-magnetosonic flows, the presence of shocks in flares is plausible (Aurass et al. 2002). Furthermore, some impulsive flares are also accompanied by CMEs, which are very likely to be drivers of global shock waves through the corona (Kahler et al. 2001). The time scales associated with the expansion of the global coronal shock waves are of the order of hours, i.e., much longer than the typical time scales in impulsive flares.

A way of gaining insights in the relative importance of flare-acceleration versus shock-acceleration is to deduce the temporal evolution of the source emitting particles from the corona into the interplanetary medium. The model developed in this work allows for the determination of both the injection profile and the interplanetary transport conditions of the solar NR electrons, without making any a priori assumption about the parameterization of the injection or the propagation mode of NR electrons along the IMF. The shape of the injection profiles is determined by details of both the acceleration processes and the mechanisms of release into the interplanetary medium (modeling these processes and mechanisms is beyond the scope of the present work). In the following sections, we discuss the implications of results obtained in the proposed scenario of NR electron injection and transport.

7.2.1 Injection profile and solar sources

We have studied seven NR electron events observed by the EPAM/LEFS60 telescope. We have identified two types of injection episodes in the inferred injection profiles: short (< 20 min) and time-extended (> 1 h). The injection profile of the May00, Jul00 and Oct02 events shows an initial injection episode of short duration, followed by a second much longer lasting

episode. The injection profile of the Dec01 and Sep04 events only displays a time-extended injection component. The two other events, May98 and Apr01, show an injection profile formed by several sparse short injection episodes.

The time scales associated with the expansion of the global coronal shock waves are of the order of hours, much longer than the typical time scales in impulsive flares (Chapter 1). Therefore we conclude that the short injection episodes are most probably related to flaring processes, while longer lasting episodes are most probably related to processes associated with the expanding CME.

We have compared the derived injection profiles with the timing of the associated electromagnetic (X-rays, optical and radio) emissions. We have found that, for all the studied NR electron events, the soft X-ray emission shows a smooth profile and starts few minutes earlier than the emission in the other frequency ranges. The beginning of the short injection episodes occurs within the rise phase of the soft X-ray flux. The soft X-ray emission is indicative of enhanced heating and it does not provide detailed information about the chronological order of the particle acceleration processes, as for example, hard X-rays and radio emission do. The short injection episodes deduced for the lowest electron energy channel analyzed in this work (E'2, 62–102 keV) coincide with the beginning of the type III radio emission. For five events, May98, May00, Jul00, Apr01 and Oct02, the radio emission is accompanied by hard X-ray emission that peaks in coincidence with the first electron injection episode.

Table 7.1 lists the properties of the injection components identified in the lowest energy channel (62–102 keV). In both, the upper and lower part of the table, the first column gives the date of the event. In the upper part of the table, the two following columns give the onset and duration of the short injection episode, the next column gives the injection rate and the last column gives the soft X-ray flare class. In the lower part of the table, the second and third columns give the start time and duration of the time-extended injection component, the injection rate and the plane-of-sky speed of the CME-leading edge. The time-extended injection component deduced for the May98 event is not included in the lower part of the table because the topology of the IMF could be different than the one assumed in the model and thus, the results derived may not be representative of the actual scenario (see section 6.3.3).

Comparing the injection rates of the two components, we claim that the short first episodes inject particles more efficiently than the time-extended episodes. In general, the injection rate of the short episodes is two orders of magnitude higher than the injection rate of the associated time-extended episodes. Figure 7.1(a) shows the deduced injection rate as a function of the intensity of the associated soft X-ray flare. As expected, the higher the intensity of the associated soft X-ray flare, the higher the injection rate of NR electrons. Figure 7.1(b) shows

Table 7.1: Injection rate of the derived components

| Event | Short injection episode | | | Flare |
| | Onset | Duration | Injection rate | X-ray |
Date	UT	s	e s^{-1} MeV^{-1}	class
1998 May 27	13:15	1140	3.4×10^{31}	C7.5
2000 May 1	10:20	144	2.3×10^{32}	M1.1
2000 Jul 14	10:27	72	1.2×10^{34}	X5.7
2001 Apr 15	13:47	72	8.1×10^{34}	X14.4
2001 Dec 26	–	–	–	M7.1
2002 Oct 20*	14:16	144	2.2×10^{32}	C6.6
2004 Sep 19	–	–	–	M1.9

*The second injection episode is not considered because type II radio emission was observed during the same time period.

| Event | Time-extended injection episode | | | CME |
| | Onset | Duration | Injection rate | Plane-of-sky speed |
Date	UT	h	e s^{-1} MeV^{-1}	km s^{-1}
2000 May 1	10:36	1.2	2.6×10^{30}	1360
2000 Jul 14	11:10	2.2	2.5×10^{32}	1674
2001 Apr 15	16:05	0.6	5.0×10^{32}	1199
2001 Dec 26	05:23	3.4	7.3×10^{31}	1446
2002 Oct 20	15:28	2.3	4.3×10^{30}	1011
2004 Sep 19	17:05	3.4	1.4×10^{31}	–

the injection rate of the time-extended periods as a function of the plane-of-sky speed of the CME-leading edge. No correlation is found, since the number of events is small and this injection rate can depend on variables not considered here such as the actual speed of the shock (not affected of projection effects) and time.

We have found that the occurrence time of the first short injection episode is not the same among the three energy channels modeled. The differences are always smaller than 5 minutes and the higher the energy the later the onset of the injection. At this stage of the study, we cannot claim that this delay has physical implications and that it is in agreement, for example, with the results obtained by Wang et al. (2006) (i.e. their Figure 3), although we cannot exclude it either. This point should be carefully studied in the future in order to identify whether or not the method produces such bias, for example due to the fact that each energy channel is independently fitted.

Reames (1999) proposed that particles accelerated in a flare are injected onto a few open field lines adjacent to the closed loop where the solar flare occurs. This implies that electrons released from flare processes can only be observed from a location magnetically well-connected with the solar flare region (±20°). Reames (1999) proposed that if a CME-driven
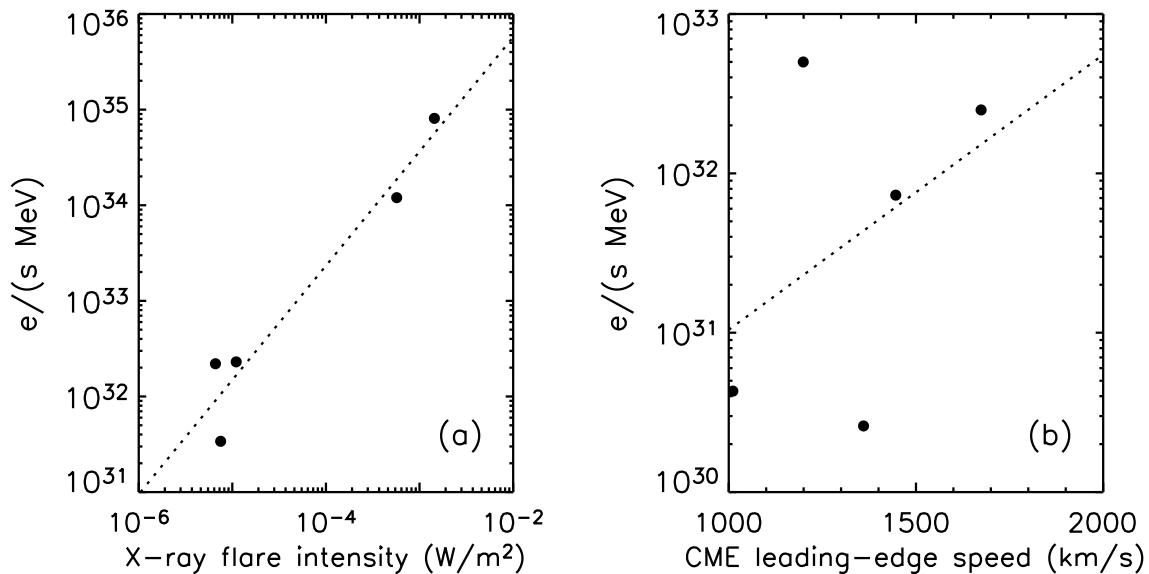
Figure 7.1: (a) Injection rate of the first short injection component versus the intensity of the associated soft X-ray flare. (b) Injection rate of the time-extended injection component versus the CME leading-edge speed.

shock is present and able to accelerate SEPs, these particles can be observed from a broad range of longitudes with respect to the parent solar event site (see Figure 7.2).

In a recent study, Wibberenz & Cane (2006) investigated the longitudinal extent of flare acceleration by studying small proton-poor 300–800 keV electron events observed by the two *Helios* spacecraft. They found prompt detectable electron increases distributed in angular distances from the flare over a range of ±80°, markedly larger than the range ±20° reported by Reames (1999) for [3]He-rich events. Therefore, Wibberenz & Cane (2006) suggested that the very narrow cone of emission quoted for the [3]He-rich events greatly underestimates the cone of emission for flare particles in general.

For the seven NR electron events analyzed in this work, we have used the average measured solar wind speed to calculate the nominal footpoint of the Parker spiral connecting *ACE* to the Sun. Next, we have calculated the longitudinal angular displacement with respect to the heliolongitude of the Hα flare (Δ). The associated solar flares were found to be all in the western hemisphere and usually magnetically well connected to *ACE* (Δ < 40°). We have observed injection episodes related to the flare for most of the events[1], which is in agreement with the results obtained by Wibberenz & Cane (2006). The exception are the events only showing a time-extended component in the deduced injection profile (Dec01 and Sep04).

The electron injection profile of the Sep04 event, one of the two events showing only one

---

[1] Always assuming, as usual, that the determination of the IMF connection occurs under stable solar wind conditions.
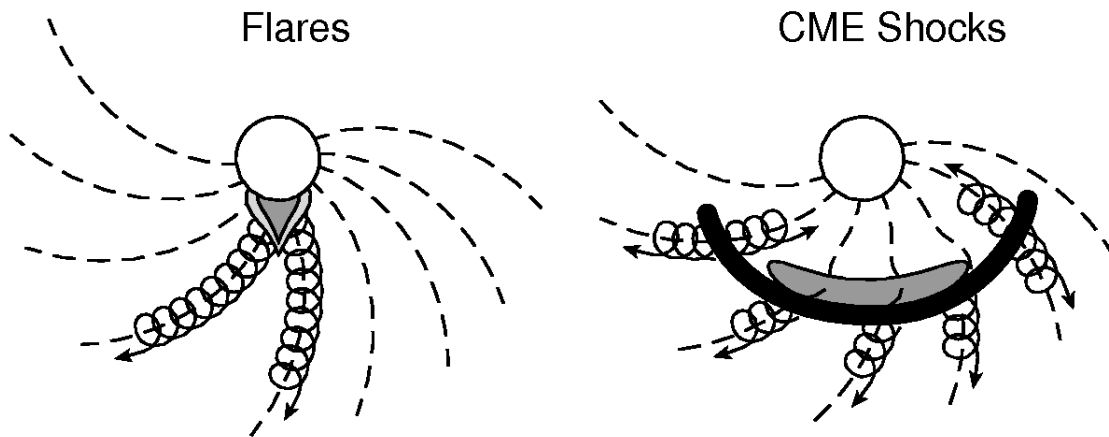
Figure 7.2: Sketch of the injection angular extent of flares and CME-driven shocks (from Reames 1999)

time-extended injection, was accompanied by type III and hard X-rays emission. No Hα flare was reported. Nevertheless, Cane et al. (2006) identified the location of the flare at N03W58 based on the observed solar active regions, leading to $\Delta = 6°$. The simulations performed for this event do not yield any short injection episode that could be associated with these electromagnetic emissions. In the case that such first injection episode existed, we would have to conclude that the longitude of the active regions did not represent the mean longitude of open field lines or its location was not well determined.

Hard X-ray bursts were not observed in association with the Dec01 event, the other event showing only one time-extended electron injection. A type III radio burst was observed, followed by a very strong metric type II burst showing clear fundamental and harmonic bands. Since type II radio bursts are the most prominent indicators of traveling shocks in the corona (Klein 2006), this suggests that NR electrons were accelerated by the CME-driven shock in the Dec01 event.

All the studied electron events were associated with CMEs observed as projections over the west limb. Five of them were wide ($>60°$) and fast (>900 km s^{-1}) enough (see Table 5.4) to drive shocks (Gopalswamy et al. 2001). Narrow ($<60°$) fast (>1000 km s^{-1}) CMEs were observed in association with well connected electron events with $\Delta < 26°$. By comparing the timing of the beginning of the time-extended injection components and the CME height-time plots observed by LASCO C2 and C3 coronagraphs, we found that, on average, the electron injection started when the CME leading-edge was at ~4 $R_\odot$.

For four events of the set, Jul00, Apr01, Dec01 and Sep04, Cane et al. (2006) reported the passage of an interplanetary shock at *ACE*. We found that three of these events (Jul00, Dec01 and Sep04) showed a clear time-extended injection component. Table 7.2 lists the

Table 7.2: Interplanetary shocks

Event	CME	Shock	Injection rate
Date	Plane-of-sky speed km s^{-1}	Transit speed km s^{-1}	e s^{-1} MeV^{-1}
2000 Jul 14	1674	1600	2.5×10^{32}
2001 Dec 26	1446	570	7.3×10^{31}
2004 Sep 19	–	690	1.4×10^{31}

plane-of-sky speed of the associated CMEs, the shock transit speeds derived by Cane et al. (2006) and the electron injection rate derived from the best fit injection profile in the lowest energy channel. With only three events it does not make sense to draw any conclusion, except for the fact that the shock with the highest transit speed displays the highest injection rate. Cane et al. (2006) suggested that transit speed can be good indicator of the shock efficiency in particle acceleration. Even with more events to compare, most probably the shock transit speed would not reflect this efficiency if we study the injection of NR electrons when CMEs are at heights lower than 30 $R_\odot$ from the Sun , because fast shocks decelerate between the Sun and 1 AU.

Cane et al. (2006) reported Fe to O abundance ratios normalized to the average value derived by Reames (1998) for 49 large SEP events in the energy range 5–12 MeV nucl^{-1} (Fe/O = 0.134). Cane et al. (2006) assumed that Fe/O > 2 indicates events with an average composition that includes a significant contribution of flare-accelerated particles, whereas Fe/O < 1 indicates events with an average composition below the typical coronal values. Cane et al. (2006) reported the Fe/O ratio for four of our selected electron events; Table 7.3 lists, from left to right, the event date, the event-averaged Fe/O ratio (normalized to 0.134) and the summing interval used for the calculation of Fe/O. According to these authors, the Apr01 and the Dec01 events included flare-accelerated particles, but not the Jul00 and the Sep04 events.

We have obtained short injection episodes for the Apr01 event related with the flare electromagnetic emissions, in accordance with a high Fe/O ratio. On the other hand, we have found a single long injection episode for the Dec01 event, lasting at least three hours. A way of explaining the high Fe/O ratio reported by Cane et al. (2006) could be that flare particles were shock accelerated remnants from previous small flares, as it has been pointed out by several authors (e.g. Mason et al. 1999; Tylka et al. 2005; Sandroos & Vainio 2007). We have also obtained a single long injection episode for the Sep04 event that seems to be related to a CME-driven shock. In this case, the low Fe/O would be indicative of particles accelerated by the CME-driven shock. Finally, the injection profile of the Jul00 event was found to consist of two injection episodes (section 6.4.3); an initial episode of short duration, followed by a

Table 7.3: Normalized Fe/O ratios[*]

| Event | Particles | |
Date	Fe/O ÷0.134	Summing Interval
2000 Jul 14	0.62 ± 0.14	Jul 14 11.0–Jul 18 19.0
2001 Apr 15	5.79 ± 0.15	Apr 15 14.0–Apr 18 00.3
2001 Dec 26	4.94 ± 0.10	Dec 26 05.5–Dec 28 22.7
2004 Sep 19	1.60 ± 1.10	Sep 19 17.2–Sep 20 17.2

[*]from Cane et al. (2006)

second much longer lasting episode. As already mentioned, the first injection episode could be related to the solar flare but it represents only the ~28% of the whole injection profile (lasting at least three hours and a half approximately). Thus, it seems plausible that flare-accelerated particles could be masked in the event averaged abundances. Cane et al. (2003) examined composition intensity profiles, not just event-averaged abundances, and they found events that showed an Fe-rich component in the beginning of the event followed by an Fe-poor component at shock passage as might be expected if there is an Fe-rich flare component in large events. In fact, the event 12–60 MeV nucl^{-1} Fe/O ratio decreases throughout the event from an initial value of about three times its typical value to a value of an order of magnitude lower (e.g. Figure 7 in Smith et al. 2001).

7.2.2 Interplanetary transport conditions

In the inner solar system, the propagation of NR electrons is governed by the particle streaming along the magnetic field lines, the scattering processes off the fluctuations of the magnetic field and the magnetic focusing in the outward decreasing magnetic field. In the developed transport model, we have used the radial mean free path, λ_r, as a measure of the degree of interplanetary scattering. From the fit of seven NR electron events, we have found that two events (May00 and Oct02) could be characterized by $\lambda_r = 0.9$ AU, whereas five events (May98, Jul00, Apr01, Dec01 and Sep04) showed $\lambda_r \leq 0.2$ AU. Those events with short rise times (< 15 min) were related to the long radial mean free path; the other ones, with longer rise times (> 1 h), were related to small radial mean free paths.

Five events (May98, May00, Apr01, Dec01 and Oct02) could be best fit if μ-dependent scattering with $\epsilon = 0.01$ was assumed; the other two (Jul00 and Sep04) required isotropic pitch-angle scattering. Local scattering conditions could be estimated from observable plasma parameters such as magnetic field strength, density and temperature of the plasma (Dröge 2003). An estimation of the scattering conditions in the heliosphere, however, remains a ma-

jor obstacle due to our lack of knowledge of the exact decomposition of the magnetic field fluctuations, which is difficult to obtain from single spacecraft measurements. Another question is how representative near-Earth measurements are for scattering conditions experienced by particles in the inner heliosphere (Dröge 2003).

Haggerty & Roelof (2002) and Haggerty et al. (2003) presented a total of 113 NR electron events observed by *ACE*/EPAM from 1997 August through 2002 March that they classified as scatter-free due to the field aligned (beam-like) PADs observed at the onset of the event. This selection of events was extended through 2005 November and the list was made available through the *ACE* Science Center web page[2]. Haggerty & Roelof (2002) identified beam-like PADs by plotting the intensity of each sector (normalized to the sector maximum) versus the mean cosine of the electron pitch-angle scanned by each sector. Haggerty & Roelof (2002) pointed out that if the sectored angular distribution has an HWHM[3] comparable to the opening half-angle of the collimator ($24°$), then the actual beam is probably as narrow or even narrower than the collimator itself.

Three of the events studied here (May00, Oct02 and Sep04) are in this list of beam-like electron events. For two of them (May00 and Oct02) we derived an electron radial mean free path of $\lambda_r = 0.9$ AU, whereas for the Sep04 event we obtained $\lambda_r = 0.2$ AU. The top panel of Figures 7.3 and 7.4 show the 102–175 keV electron spin-averaged intensities for the Oct02 and the Sep04 events, respectively. The bottom panels of these figures display selected PADs showing eight snapshots of the evolution of the electron distributions. The snapshots are labeled from (a) to (h) and correspond to the times marked by dots in the top panels. These can be considered representative of the different phases of the electron events (onset, rising phase, peak and decaying phase). In each snapshot, the numbers 1–8 give the intensity measured in each sector of the LEFS60 telescope normalized to the intensity of the peak sector (with the pre-event electron intensity subtracted). The dotted lines show the PADs predicted by the model, also normalized to the maximum.

Observational sectored angular distributions like the ones shown in Figures 7.3(b)–(c) and 7.4(a)–(b) have been understood to provide the canonical signature for a field-aligned beam and they have been used to describe the events as scatter-free (Haggerty & Roelof 2002). Nevertheless, it is clear from these figures that although the distribution of the first group of particles is beamed at the arrival, both the evolution of the PADs and the total duration of the events is very different.

Earl (1976) studied the propagation of charged particles under adiabatic focusing and pitch-

---

[2]List of beam-like electron events as observed by the *ACE*/EPAM instrument:
  `http://www.srl.caltech.edu/ACE/ASC/DATA/level3/epam/CorrectedBeamList.pdf`
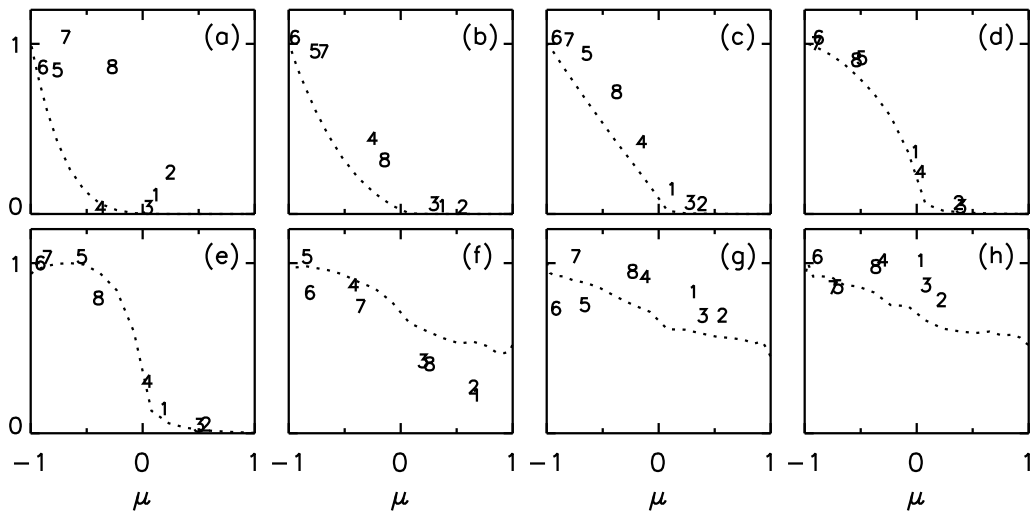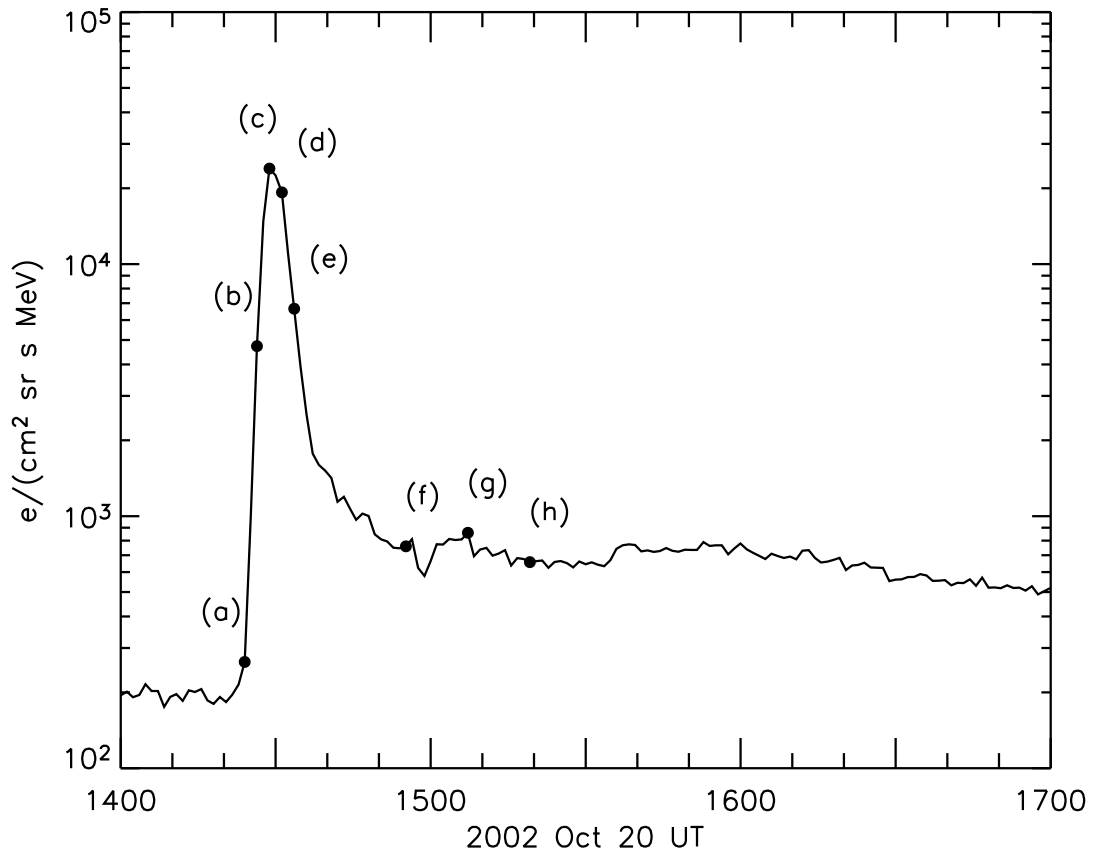[3]Half Width at Half Maximum

Figure 7.3: Top: spin-averaged 102–175 keV electron intensity observed by EPAM/LESF60 on 2002 October 20. Bottom panels: observational sectored angular distributions normalized to maximum (1–8) and corresponding simulated PAD (dotted curve) for eight selected snapshots – from (a) to (h) –.
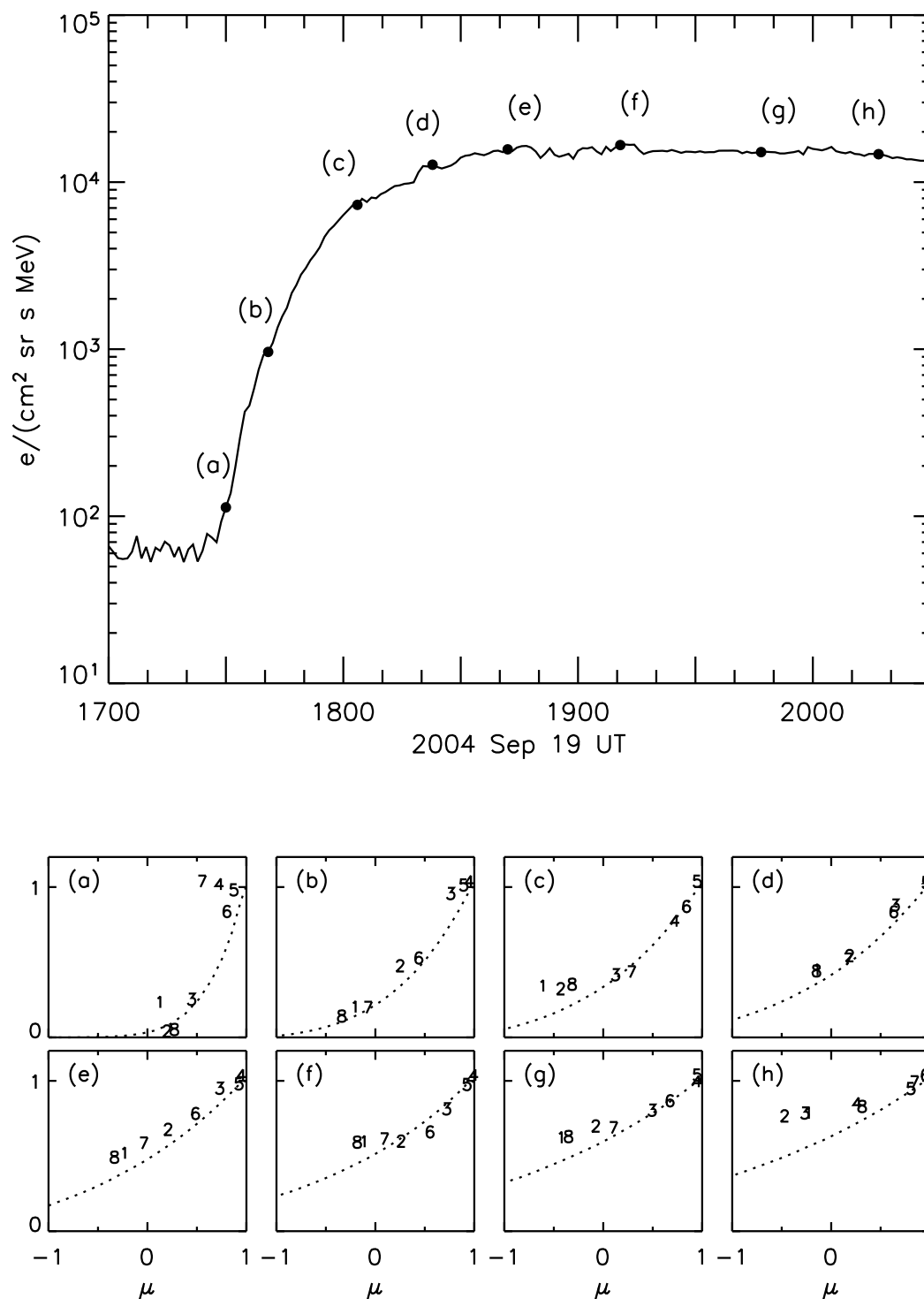
Figure 7.4: Top: spin-averaged 102–175 keV electron intensity observed by EPAM/LESF60 on 2004 September 19. Bottom panels: observational sectored angular distributions normalized to maximum (1–8) and corresponding simulated PAD (dotted curve) for eight selected snapshots – from (a) to (h) –.

175

angle scattering effects and derived explicit formulae to describe, for two different regimes, the particle density profile that results from a localized impulsive injection. Earl (1976) found that in the first regime, when focusing is strong, the propagation is purely coherent. In the second regime, when focusing is relatively weak, the diffusive mode of propagation is dominant but coherent modes are also present at the beginning of the event.

Wibberenz & Cane (2006) expressed the same idea in other words. They stated that the mean free path should not be understood as the distance that each individual particle travels along the IMF before it is scattered back. Early in a solar particle event the backscattering of particles may be very small. This leads to the "beamed" arrival of the first group of particles. Later in the event, those particles that have been scattered by the IMF fluctuations arrive at the observer completing the event. In the terminology of Earl (1976), first we detect the "coherent peak" and later the "diffusive wake". Thus, the term "scatter-free event" should be used with some care.

For some events, it is also possible to propose an alternative scenario where particles propagate scatter-free from the Sun to 1 AU and be scattered back at some distance beyond 1 AU. The first particles would be observed as a "coherent peak" whereas the rest of the event would consist of a mixture of particles scattered back, mirrored close to the Sun and newly injected from close to the Sun if an extended injection exists. This scenario was not considered in our model.

Finally, just to remind that for all the events in our set, the mean μ-co was higher than 70% (see selection criteria in section 5.1). This is not necessarily the situation in many NR electron events. Even for those selected here; there are short time periods were the μ-co is smaller than 50%, at 10:40 UT on 2000 May 1 (Figure 5.2), at 17:35 UT on 2004 September 19 (Figure 6.2), at 05:57 UT on 2001 December 26 (Figure 6.7) and at 16:28 UT on 15 April 2001 (Figure 6.21), for example. Low coverage in pitch-angles during long time intervals could lead to a wrong determination of the mean free path and the conditions of particle propagation in interplanetary medium.